

The eclipsing LMC star OGLE05155332-6925581: a clue to understand Double Periodic Variables

R.E. Mennickent,^{1*} Z. Kołaczowski^{1,2}, G. Michalska², G. Pietrzyński^{1,3}, R. Gallardo¹, L. Cidale⁴, A. Granada⁴, W. Gieren¹

¹Universidad de Concepción, Departamento de Física, Casilla 160-C, Concepción, Chile

²Instytut Astronomiczny Uniwersytetu Wrocławskiego, Kopernika 11, 51-622 Wrocław, Poland

³Warsaw University Observatory, Al. Ujazdowskie 4, 00-478, Warsaw, Poland

⁴Facultad de Ciencias Astronómicas y Geofísicas, Univ. Nacional de La Plata and Instituto de Astrofísica La Plata (IALP), CONICET, Paseo del Bosque S/N, 1900, La Plata, Ar.

ABSTRACT

We investigate the nature of the eclipsing variable OGLE05155332-6925581, one of the brightest members of the enigmatic group of Double Periodic Variables (DPVs) recently found in the Magellanic Clouds. Its nature is revealed through the analysis of new optical and infrared spectroscopy and the study of its archive long-term photometry. We apply a Fourier disentangling method to completely separate both periodic components found in the light curves (LCs) and hence to study separately the orbital and long-term phenomena. The modeling of the MACHO, OGLE II and III orbital LCs, along with the analysis of the radial velocities curves suggest that this object is a semi-detached binary with the less massive star transferring matter to the more massive and less evolved star, in an Algol-like configuration. We find also wavelength dependent systematic differences between solutions for system parameters. Detailed comparison between adopted models and observed orbital changes provides evidence for additional orbital variability likely caused by an accretion disc around the primary and presence of a third light in the system. As in the case of β Lyr the circumprimary disc seems to be more luminous than the primary, but we do not detect orbital period changes in OGLE05155332-6925581. We find that accretion is not the main powering mechanism for the circumprimary disc. The spectral energy distribution shows a remarkable infrared excess at the *I* band increasing beyond $2.2\ \mu\text{m}$. A change in the long period from 188.2 to 172.5 days in a time interval of ~ 1100 days is documented. We find that the LC follows a loop in the color-magnitude (CM) diagram during the long cycle; the system is redder when brighter and the rising phase is bluer than during decline. The source of the long-term periodicity is not eclipsed, indicating its circumbinary origin. Strong asymmetries, discrete absorption components (DACs) and a γ shift are new and essential observational properties in the infrared H I lines. The DACs strength and RV follow a saw-teeth pattern during the orbital cycle. Helium lines are quite variable in shape and strength and appear mostly during superphases 0.3–0.8. We suggest that the system is at the end of a rapid mass exchange stage and poses an outflowing circumbinary disc responsible for the infrared excess and long-term variability. The DAC pattern can be interpreted as the spectral signature of accelerating gas streams flowing through the Lagrangian L_2 and L_3 points. The loop in the CM diagram is similar to that observed in Be stars by de Wit et al. (2006), and it could reflect quasi-cyclic episodes of circumbinary disc creation/dissipation. We argue that the above scenario could be applied to the DPVs as a class, and conclude that DPVs could be a new type of rather massive semi-detached systems characterized by mass exchange, luminous circumprimary discs, episodes of mass loss and circumbinary disc formation. The study of DPVs could constraint non-conservative models of binary star evolution.

Key words: binaries: eclipsing, stars: early-type, stars: evolution, stars: mass-loss, stars: variables-others

* E-mail: rmennick@astro-udec.cl. Based on observations carried out at

ESO and CTIO telescopes: ESO proposal 076.D-0126(A) and NOAO proposal G014E03B.01

1 INTRODUCTION: ABOUT DPVS AND OGLE05155332-6925581

The star OGLE05155332-6925581 (MACHO IDs 79.5739.5807 and 78.5739.78; OGLE LMC-SC8-125836) is a member of the group of close binaries named Double Periodic Variables (Mennickent et al. 2003, Mennickent et al. 2005a). These stars show two closely related photometric periodicities; the shorter one reflects the binary period but the cause for the longer periodicity (or quasi-periodicity since it is not exactly cyclic, Mennickent et al. 2005b) still is unknown. We have selected OGLE05155332-6925581 for a detailed monitoring and study since it is relatively bright, has a large amplitude of the long term changes and its eclipsing nature could help to shed light on the nature of the phenomenon of Double Periodic Variables, especially their evolutionary stage and long-term variability.

OGLE05155332-6925581 shows a long term periodicity of 188 day and an eclipsing variability with orbital period 7.2843 days (Mennickent et al. 2003). The standard multi-color photometry of this system is available in several catalogues published recently. Zaritsky et al. (2004) gives simultaneous $U = 15.040 \pm 0.032$, $B = 15.575 \pm 0.031$ and $V = 15.587 \pm 0.057$ mag. Wyrzykowski et al. (2003) gives $V = 15.38$, $B = 15.32$ and $I = 15.27$ mag at maximum. Ita et al (2004) provides single-epoch simultaneous three color infrared imaging with $J = 15.586$, $H = 15.566$ and $K_s = 15.490$ mag. No epoch is available for these measurements. OGLE05155332-6925581 is one of the brightest DPVs in the LMC, in consequence the quality of the available photometry is good enough for concluding about physical properties of this object. On the other hand, their photometric credentials are typical for DPVs so it can be considered as a representative case.

OGLE05155332-6925581 appears in the field as a visual double, with a nearby companion $3.8''$ to the East. This neighboring star was also observed photometrically and spectroscopically. The OGLE position for the companion is RA= 05:15:53.88 and DEC= -69:25:58.1 and the photometry gives $V = 16.947$, $(B - V) = 1.812$ and $(V - I) = 1.821$ mag. The I -band light curve (LC) consisting of 395 datapoints gives a mean of $I = 15.072$ mag with RMS 0.006 mag. 2MASS data for this star give $J = 13.928 \pm 0.048$, $H = 13.046 \pm 0.061$ and $K = 12.817 \pm 0.055$ mag. A finding chart based on an OGLE image taken at the I -band is given in Fig. 1.

We provide a description of our observations and archive photometric data in Section 2 along with our methods of data reduction and analysis. The results of our LC modeling and spectroscopic study are given in Section 3 and a discussion is presented in Section 4. Our conclusions are given in Section 5.

2 SPECTROSCOPIC OBSERVATIONS AND SOURCES OF PHOTOMETRY

We have monitored OGLE05155332-6925581 spectroscopically in the optical wavelength range during August 2003 and February 2004, and in the infrared region during December 2005 and December 2006 and also obtained an optical high resolution spectrum at a single epoch in 2007. In this section we give details of these observations. In addition, we have used public domain photometric data available from the MACHO (Allsman & Axelrod 2001) and OGLE II databases (Udalski et al. 1997, Szymański 2005) along with OGLE III data. The MACHO light curves analyzed in this paper consist of 1469 photometric measurements obtained at the "red" filter (central wavelength 7000 Å) and 1555 measure-

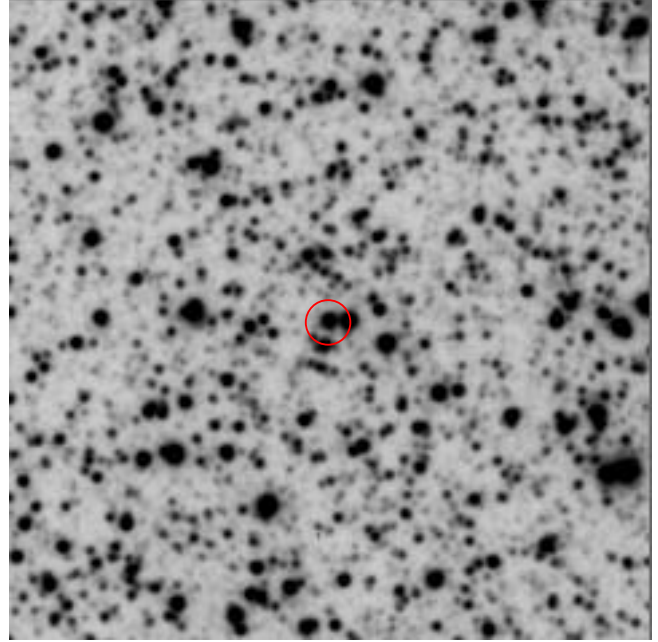


Figure 1. The finding chart of OGLE05155332-6925581. North is up and east right. The field of view is $1'.7 \times 1'.7$ and centered at RA(2000)= 05:15:53.32 and DEC(2000)= -69:25:58.1. The circle indicates the position of OGLE05155332-6925581.

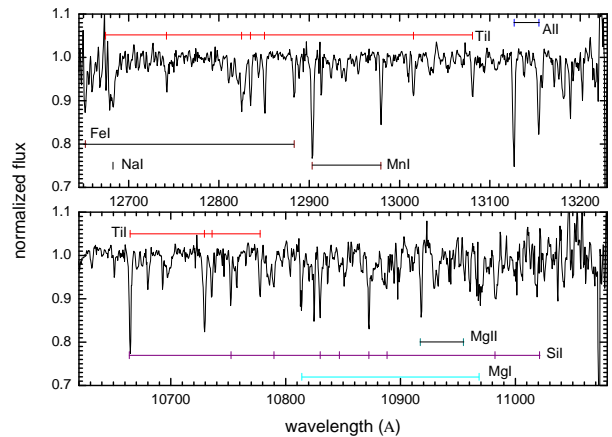


Figure 2. The average infrared spectra for the nearby companion observed in the same slit. Equivalent total exposure time is 3.3 hours. The spectra have been corrected by the stellar radial velocity. Line identification is based on the work by Wallace et al. (2000).

ments obtained at the "blue" filter (central wavelength 5200 Å) during HJD 2 448 826.136 and 2 451 536.193 (red) and 2 451 541.999 (blue). We also analyzed 896 OGLE II and III magnitudes obtained at the I -band (central wavelength 8000 Å) spanning a time interval between HJD 2 450 457.649 and 2 453 823.498. The total time covered by the photometric data analyzed in this paper is 13.7 years.

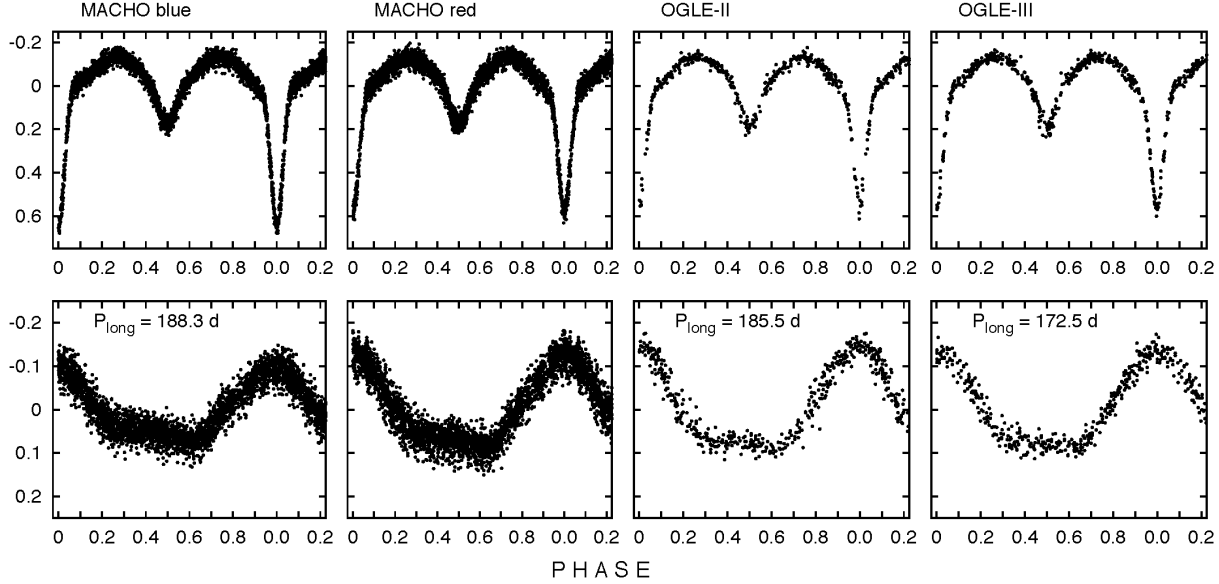


Figure 3. Results of the Fourier light curve decomposition showing the orbital and long-term variability separately.

Table 1. Radial velocities for OGLE05155332-6925581 in km/s referred to the Local Standard of Rest. HJD' means HJD-2 450 000. Orbital and super-phases are given along with detection d of He I 4471 (p: positive, w: weak, w: weak doubtful and n: negative).

UT-date	HJD'	Φ_o	Φ_s	H δ	H γ	H β	d
Aug08	2859.8912	0.582	0.074	226	154	208	n
Aug20	2871.8437	0.222	0.144	-	-	-	n
Sep03	2885.7998	0.138	0.225	293	308	328	n
Sep11	2893.7845	0.235	0.271	366	410	357	n
Sep24	2906.8188	0.024	0.346	359	366	312	w
Sep26	2908.8315	0.300	0.358	508	295	459	p
Oct10	2922.8309	0.222	0.439	408	430	316	w
Oct22	2934.7777	0.862	0.508	207	212	185	p
Oct24	2936.7097	0.127	0.520	142:	320	240	w
Nov27	2970.8199	0.810	0.717	132	229	215	w:
Nov28	2971.7277	0.935	0.723	225	191	231	p
Dec10	2983.7592	0.586	0.792	101	136	244	p
Dec11	2984.7069	0.716	0.798	205	103	241	n
Dec12	2985.6706	0.849	0.803	219	164	165	n
Dec17	2990.7294	0.543	0.833	217	306	274	n
Dec18	2991.7520	0.684	0.839	235	269	148	w:
Dec19	2992.7313	0.818	0.844	109	166	155	w:
Dec30	3003.6639	0.319	0.908	346	378	397	n
Dec31	3004.6364	0.452	0.913	290	274	248	w:
Jan11	3015.6778	0.968	0.977	267	268	241	n
Jan12	3016.6215	0.098	0.983	-	467	448	n
Jan20	3024.7157	0.209	0.030	391	451	471	n
Jan21	3025.6757	0.341	0.035	391	267	405	p
Jan22	3026.6209	0.471	0.041	256	253	347	p
Jan31	3035.6290	0.707	0.093	116	182	95	p
Feb01	3036.6371	0.846	0.099	164	67	131	p

2.1 Time resolved optical spectroscopy

26 spectra of OGLE05155332-6925581 in the wavelength region of 3900–5300 Å were obtained with the 1.5m CTIO telescope in service mode using the Cassegrain Spectrograph with grating 26

tilted 15°94. The slit width of 1'' yielded a nominal resolution of 2 Å. He-Ar comparison spectra obtained along every science exposure provided wavelength calibration functions with typical rms of 0.1 Å (6 km/s at H β). In the spectra we measured the radial velocity (RV) of the Balmer lines with simple gaussian fits. The average RV of the standard star LTT 2415, measured every observing night, resulted to be 255 ± 36 km/s, which compares well with the value of 253.4 km/s reported in the SIMBAD database. Our measured velocities for OGLE05155332-6925581 are given in Table 1.

2.2 The MIKE high resolution spectrum

We obtained one spectrum of OGLE05155332-6925581 with MIKE in the Bade Magellan telescope of Las Campanas Observatory, Chile, the night of February 23 (UT), 2003 (UT-start 00:58:39, HJD at mid-exposure 2 452 693.55208). We used a 1800 sec exposure and a slit width of 0.35 arcsec, resulting in a resolving power $\sim 70,000$. Our spectrum was taken at orbital phase 0.756 and super-phase 0.110 (see below). The standard calibration and extraction of the spectrum with IRAF tasks was applied. The spectrum was wavelength calibrated with several hundreds comparison lines of ThAr spectra taken before and after the exposure. The RMS of the calibration function was about 10^{-3} Å.

2.3 J-band infrared spectroscopy with the ESO ISAAC

Our observations were conducted at the ESO Paranal observatory with ISAAC in the SW-MR mode in service mode. The detector was the Hawaii Rockwell array with nominal gain 4.5 e/ADU and readout noise 11 electrons. This spectroscopic mode provided a plate scale of 0.147'' per pixel. We used a slit width of 1'' yielding a spectral resolution of 2.4 Å and resolving power $R \approx 4550$. We observed OGLE05155332-6925581 at three different spectral regions: the j region between 1.061–1.108 μm , the sz region between 1.154–1.215 μm and the jplus region between 1.265–1.324 μm .

Table 2. Observing log for the infrared spectroscopy. We give the exposure time in seconds T , the observing block name, the seeing value as measured in the acquisition image (s1) and read it from the image header (s2), in arcseconds, and the spectral band. NA means not available.

date(UT)	$T/4$	MJD	OB	s1-s2	band
21-22/12/05	600	3726.2744-3726.2958	051221	0.64-0.93	j
10-11/01/06	600	3746.1699-3746.1913	205091	0.54-0.68	j
10-11/01/06	600	3746.1992-3746.2205	205094	NA-0.69	sz
11-12/01/06	500	3747.1895-3747.2074	205088	0.58-0.79	jplus
11-12/01/06	600	3747.2141-3747.2355	205092	NA-0.56	j
15-16/02/06	600	3782.1062-3782.1276	205095	0.60-0.69	sz
16-17/02/06	600	3783.0996-3783.1209	205097	0.57-0.92	jplus
14-15/04/06	600	3839.9825-3840.0038	205093	0.69-0.78	j
17-18/03/06	500	3811.9970-3812.0150	205090	0.60-0.83	j
12-13/10/06	600	4021.2740-4021.2954	205098	0.75-1.32	jplus
09-10/11/06	600	4049.3222-4049.3435	205099	0.56-0.45	jplus
06-07/12/06	600	4076.2686-4076.2899	255548	0.66-1.36	jplus

The observations were done as usual in the infrared, with the technique of dithering. This method consists in observing the object at two or more positions along the slit. The sky is effectively removed by subtracting one frame from the other, registering the two beams and then subtracting again. First steps of image reductions like geometrical distortion correction, flat fielding and bias removal were done by the ISAAC pipeline software at the observatory. The wavelength calibration was done identifying night sky lines in the image and building a wavelength calibration function for every spectrum. Extraction was done with the usual IRAF tasks.

We used a generic template of infrared atmospheric lines to remove telluric lines. This template was rebinned and resolution degraded to match the characteristics of our spectra. Then we divided the science spectra by the telluric spectrum after finding the best wavelength shift and vertical scaling providing the best telluric feature removal. Equivalent widths were measured by line fitting with Lorentz functions. For those lines showing discrete absorptions in their wings, we deblended the profile with two Lorentz functions of variable depth and width to take into account the blending. For comparison, we also measured the equivalent width with the standard formula integrating the line flux under the interpolated continuum, yielding results about 15% lower than those obtained with the first method. For the OB205093 spectrum, only this method was possible due to the large line asymmetry. We measured radial velocities in the infrared spectra determining the wavelength at minimum of the flux. We determined an internal error of 10 km/s from radial velocities of the comparison star, red companion described in Section 1, placed in the same slit. Details of the observations are given in Table 2. We found that the comparison star is a probable member of the LMC, its RV referred to the LSR is $+246 \pm 10$ km/s. The spectra for this star are plotted in Fig. 2, along with line identifications; the star could be considered as a flux and radial velocity standard in the LMC. Using the ratio between the Mn I feature strength to that of Mg I in the formula provided by Wallace (2000) for Galactic giant stars we obtain a temperature of ~ 3953 K. We also note that the Hipparcos ISAAC telluric standards Hip 026368 and Hip 029635 are Be stars; they show double peak Pa β emission with peak separation of 205 and 235 km/s, respectively. The first star is the well known Be star AZ Dor (B9.5 Ve) and the second one (HD 44533, B8 V) is a new Be star.

Table 3. Periods and amplitudes found in the light curves.

period (d)	range (mag)	MACHO	period (d)	range (mag)	OGLE
7.28428	0.773	blue	7.28425	0.660	II
188.4	0.166	blue	185.6	0.240	II
7.28431	0.713	red	7.28430	0.651	III
188.3	0.206	red	172.5	0.220	III

Table 4. The best system parameters (p), derived assuming a stellar origin for the deeper eclipse. At every band we give the flux fraction $l_1/(l_1 + l_2)$ at maximum. Ranges for the dynamical masses are derived from the radial velocity study summarized in Table 7. For our calculations we have used published values of $\mu = 18.39$ and $E(B - V) = 0.17$.

p	MACHO blue	OGLE II	p	value
q	0.287	0.393	$Sp1$?
$\log g_1$	3.96	3.79	$Sp2$	B6 III
$\log g_2$	2.86	2.88	$M_{V,2}$	-2.83
$T_1 (K)$	25000	25000	$M_{bol,2}$	-4.03
$T_2 (K)$	14090	14330	r_2/a	0.29
$i(\text{deg})$	80.4	80.4	r_1/a	0.16
f_B	0.419	0.419	M_1	(7.1–4.2) M_\odot
f_V	0.392	0.418	M_2	(2.8–1.6) M_\odot
f_I	0.360	0.387		
f_J	0.324	0.351		
f_H	0.315	0.342		
f_K	0.308	0.335		

3 RESULTS

3.1 Photometry from OGLE and MACHO

The light curves were analyzed with a Fourier disentangling method. This allowed us to separate the Fourier amplitudes and frequencies of the two different periodic signals detected in the time series photometry. A summary of these parameters for OGLE05155332-6925581 is given in Table 3. The results of our analysis of the OGLE and MACHO photometry are displayed in Fig. 3. The light curves are folded with the orbital and the long-term period. The double eclipsing nature of the variable is evident as well as the hump-like character of the long-term light curve, whose variability is limited to half a cycle only, and shows larger amplitude at the red band. We observe the eclipses slightly deeper in the blue band. The improved ephemeris for the main

Table 5. Equivalent widths and radial velocities in the infrared spectra. Φ is the orbital phase.

OB	Φ	EW(\AA)	RV(km/s)	line
051221	0.599	3.5	330	Pa γ
205091	0.331	5.1	535	Pa γ
205094	0.336	-	-	-
205088	-	5.5	-	-
205092	0.475	5.7	334	Pa γ
205095	0.264	-	-	-
205097	0.401	7.1	447	Pa β
205093	0.210	4.2	559	Pa γ
205090	0.368	4.9	467	Pa γ
205098	0.098	5.8	461	Pa β
205099	0.948	5.9	279	Pa β
255548	0.648	4.6	229	Pa β

minimum is (the numbers in parentheses are the errors with the zeros omitted):

$$HJD_0 = 2\,450\,000.1392(21) + 7.284297(10) \times E \quad (1)$$

We note that the long-term variability source is not eclipsed. This result contradicts the finding by Mennickent et al. (2005a, hereafter M05) based on the visual inspection of the light curves phased with the orbital period for two DPVs (their Fig. 12). The apparent absence of long-term variability during the main eclipse turned to be only a visual effect produced by the large magnitude gradients found around minimum. The better treatment of the data by the Fourier decomposition technique completely separates the short and long-term variability and reveals that the visual impression is not real. Our finding suggests that the source of the long-term variability is placed around the binary system, and this is the rule for all eclipsing DPVs (Kołaczowski et al. in preparation).

In Fig. 4 we show the O-C diagram for times of maximum of the long-term variability. The maximum moments and their errors were measured at every cycle by fitting the LC with the average light-curve defined for a given band as a spline function. There is a clear change in behavior after cycle number six; the long variability becomes faster, and the O-C diagram is consistent with a period change from 188.2 d \rightarrow 172.5 d. Our data does not reveal if this transition is gradual or consist of discrete period jumps, but the O-C diagram suggests a single transition episode between sixth and twelfth cycle. The shorter period is observed during the OGLE III epoch, and we note in Fig. 3 that the shape and amplitude of the long-term light curve remains unchanged, besides the notable period change. The ephemeris for the long-term variability during OGLE III epochs is $HJD_{max} = 2\,452\,674.6 + 172.5 \times E$.

During minimum and maximum of the light the system has the most blue and red color, respectively. Fig. 5 shows the color-magnitude diagram for the long-term variability of the MACHO red light curve, indicating magnitudes taken during rising or decline from maximum. We observe a clear pattern in the diagram: the loop characterized by bluer rising than decline phase. This loop is reminiscent of that observed by de Wit et al. (2006) in light curves of outbursting Be stars in the Magellanic Clouds, and is also a strong evidence for circumbinary source of the long period variability.

3.2 Orbital light curve modeling

When we used the Wilson-Devinney (Wilson & Devinney 1971) code for modeling the eclipsing variability of OGLE05155332-6925581 we encountered essential problem with getting convergence of the solution for all available LCs. In that case we find also non-physical solutions revealed as negative third lights. Finally, we have used a light curve modeling program based on WD code that find the best solution mapping a global minimum of summed residuals in a multi parametric space using Monte-Carlo techniques (Michalska & Pigulski 2005). We conducted the search for optimal solution for every band separately applying also reliable simplifications. Circular orbits, synchronous rotation and absence of third light are assumed by this method. A fixed temperature of primary component is roughly estimated from brightness and distance of the system using the method described in Michalska & Pigulski (2005). This iterative method pick up the visual magnitude at maximum and starts assuming equal luminosities for both components and the T_1 versus M_{bol} relation for Galactic detached main-sequence eclipsing binaries published

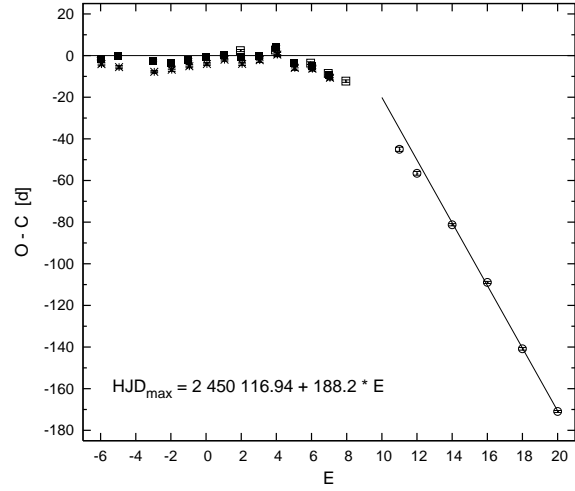


Figure 4. The O-C diagram for the maxima of the long-term variability. Filled squares correspond to MACHO-red data, asterisks to MACHO-blue data, open squares to OGLE II data and open circles to OGLE III data.

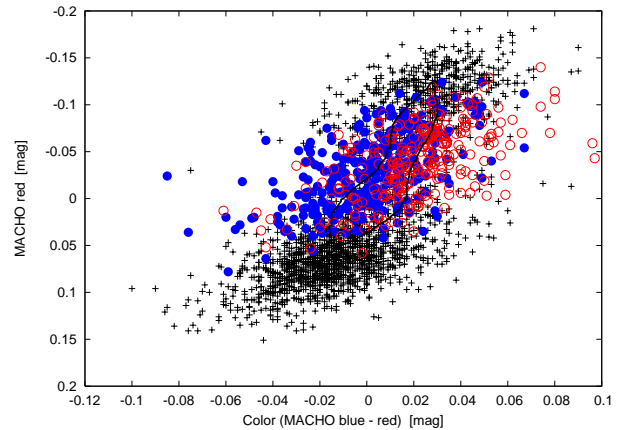


Figure 5. The color-magnitude diagram for the long-term variability in the MACHO red LC. Solid circles are magnitudes taken during the rising and open circles are those obtained during decline from maximum. Magnitudes taken at the maximum and broad minimum are shown by pluses. The loop-like solid line follows the average temporal trend.

by Harmanec (1988). The difference between the Galaxy and LMC metallicities for the parameters BC and M_V was calculated from models of Bertelli et al (1994). The T_1 value hence estimated converges to 25.000 K. The best fit parameters are given in Table 4 and the model light curves are shown in Fig. 6. Estimates of the fit quality are given in Figs. 7 and 8. We observe systematic differences between the best solutions at different wavelength bands (Figs. 7 and 8). We argue that these differences could be due to the absence of including a third light in our models. In consequence we cannot adopt these models as the conclusive physical solution, but for discussion concerning general properties of the system these results are very useful.

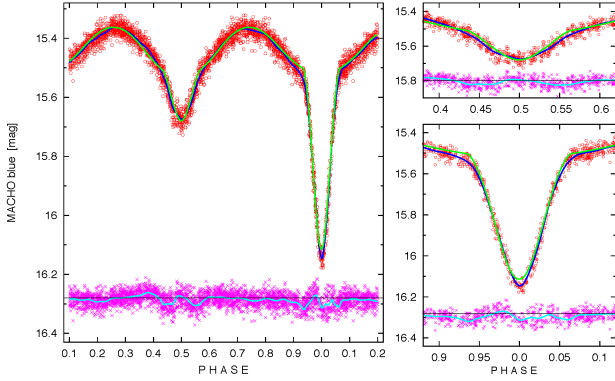


Figure 6. A detailed comparison of the model and observations. Red open circles are observations (MACHO blue; long term variability is removed), the dark blue line is the fit of spline functions to observations, the green line is the model, based on the parameters of the best solution for MACHO blue data. Magenta crosses are the observations minus model, the light blue line is the spline fit minus model. Zoomed views of eclipses are given in the right side panels.

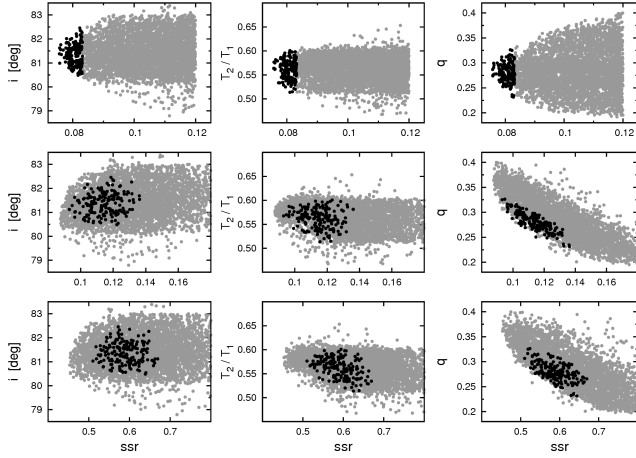


Figure 7. Results of our Monte Carlo simulations. Every point represents a model, characterized by a set of input parameters for the WD code and its sum of squares of residuals (ssr). The models in the figures are those minimizing ssr at the MACHO blue LC (upper panels). These models generate LCs at bandpasses corresponding to MACHO red and OGLE LCs. Comparison of these synthetic LCs with the observational data yield to the diagrams of the middle and bottom panels, respectively. Black dots are a 10% selection of the best models for the MACHO blue LC.

The potentials of the secondary star in whole possible range of the mass ratios clearly indicate a semi-detached configuration (Fig. 9). We find $T_1 = 25000$, $T_2 = 14090$, $\log g_1 = 3.96$, $\log g_2 = 2.86$, $i = 80^\circ.4$ and $q = 0.29$ from the best MACHO blue light curve fitting model. These parameters are well confirmed by the analysis of the OGLE II light curve except the mass ratio, for which we find $q = 0.39$. The ratio of the stellar radii R_2/R_1 is in the range 1.79 (for OGLE I-band data) to 1.91 (for MACHO blue).

The temperature and surface gravity of the secondary agree with the improved values obtained from the spectra reported by M05, viz. $T_2 = 13.500 \pm 1000$ K, $\log g_2 = 3.2 \pm 0.5$ and $M_v = -2.0 \pm 0.3$, $M_{bol} = -2.9 \pm 0.3$ and spectral type B5 IV.

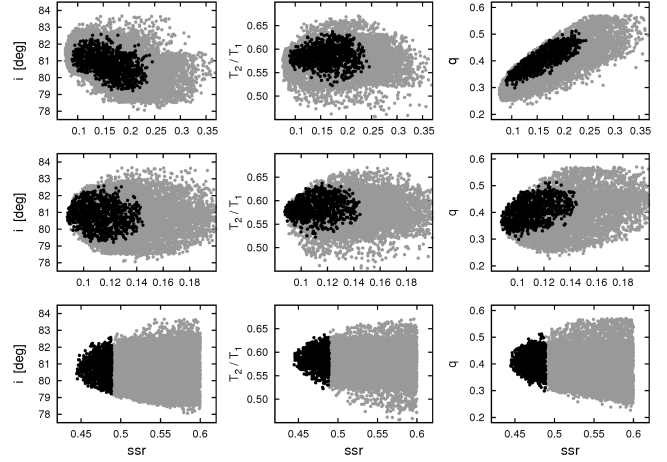


Figure 8. Same as Fig. 7 but considering models optimized for the OGLE II light curve.

Further detailed comparison between synthetic and observed LCs reveals additional component (fourth light) modulated with orbital cycle of the system. As we can see in Fig. 6 the overall model LC is quite good, but some significant deviations are present at phases of both eclipses. The system is fainter than the model at the main minimum and also during ingress and egress of main eclipse. In addition, the observed secondary eclipse is wider than the model. These features on the observed LC could be explained by the presence of an optically thick disc of gas around the primary star. This kind of accretion structure can be present in the system with mass transfer from secondary to primary star. The deeper minimum is the opposite effect that expected in the presence of the third light. In the observed eclipses both additional components, third and fourth light, should have a contribution in opposite directions, but in our simple modeling is impossible to estimate their total influence. We will return to the LC interpretation in the discussion section.

3.3 The infrared spectra: DACs and γ shifts

We show in Fig. 10 and 11 the smoothed (7-point average) $\text{Pa}\beta$ and $\text{Pa}\gamma$ hydrogen lines for OGLE05155332-6925581. Equivalent widths and radial velocities are given in Table 5. Our 10 spectra cover well the orbital phases between 0.95 and 0.65 but not the phases between 0.65 and 0.95. The HI lines appear in absorption with variable asymmetries and depths; the depth is larger at phases 0.37-0.40 and smaller at phases 0.60-0.65. The HI profiles looks quite complex in structure. We identify the main absorption with the secondary star (see Section 3.4) but there is a weaker and wider absorption component in the HI lines appearing in some phases which we attribute to the primary star. In Fig. 12 we show the non smoothed $\text{Pa}\beta$ spectrum at phase 0.47, along with a synthetic binary absorption profile built considering the stellar parameters found in Section 3.2. In order to reproduce the observed $\text{Pa}\beta$ profile, we consider the contribution of a primary star with $T_{eff} = 25000$ K and $\log g = 4$ and a secondary star with $T_{eff} = 14000$ K and $\log g = 3$. For each object we assumed that the photosphere is in radiative and hydrostatic equilibrium and is represented by the corresponding density and temperature distributions given by Kurucz's (1979) model atmospheres. The line profiles are obtained by solving the transfer equation and the equations of statistical equilibrium for multi-level atoms in the comoving frame with the

ETLA code (as described by Catala & Kunasz, 1987). We assumed a spherically symmetric slowly expanding atmosphere with a mass loss rate 10^{-9} solar masses per year. The ETLA code was modified in order to deal with a hydrogen model of 23 bound energy levels and a continuum. Once the line source function was known, the line profiles for the primary and secondary stars were computed in the observer's reference frame. Then, they were convolved with a rotational profile with $v \sin i$ of 400 km/s and 100 km/s, respectively. Finally, we summed up both contributions in order to fit the line profile of $\text{Pa}\beta$ of the binary system. It is notable the high velocity required to fit the primary star spectrum, viz. 400 km/s. This fact shows that the primary rotates very fast, non-synchronously and probably at critical speed (see Section 3.5). We do not observe emission lines in the studied infrared spectral regions.

We find transient absorption features around λ 1.084, 1.093 and 1.280 μm . We have identified the feature around λ 1.084 μm with He I 1.083 μm . During orbital cycle this line is quite variable in strength and shape; it is stronger and wider at phases 0.33 and 0.37 and disappears in the spectrum of phase 0.21. Their RV is confusing, it follows $\text{H}\gamma$ except at phases 0.33 and 0.37 when is bluer and stronger. The other two absorption features are much narrower and placed at the blue side of the H I lines, with velocities between 550 and 850 km/s from the line center. The feature close to 1.093 μm is specially interesting; it appears in emission at phase 0.37, as a mini P-Cygni profile at phase 0.33 and as absorptions at phases 0.48, 0.60 and 0.21 (the phases are not of the same cycle number). The good removal of telluric lines in the region 1.086-1.092 μm illustrated in Fig. 10 suggests that the transient features are real and not artifacts of the process of telluric correction. The only pair of $\text{Pa}\beta$ and $\text{Pa}\gamma$ profiles obtained the same night are those obtained at phases 0.47 and 0.48. In this case the $\text{Pa}\gamma$ narrow absorption does not appear in $\text{Pa}\beta$, but this could be due to the fact that the line is rather weak and that not necessarily the transients should appear with the same strength in all lines of the Paschen series. It is possible that the narrow blue side emissions could be related to the emissions observed at the red wing of the $\text{Pa}\gamma$ profile at phases 0.60, 0.48 and 0.33 (maybe they are also present around some of the He I 1.084 lines). We note that these putative emissions do not appears simultaneously at both line flanks, except in the spectra of phase 0.33. The quality of our data is not enough to be conclusive about the reality of these emissions, but we are confident about the much well defined blue-shifted narrow discrete absorption components (DACs).

If the emission shoulders are confirmed in higher S/N spectra, they could be evidence of a rotating disc-like structure around the primary star. On the other hand, we find DACs stronger on superphases (the phases referred to the long period) 0.10, 0.76, 0.81 and 0.97, i.e. around long-cycle maxima, and weaker or absent on superphases 0.40-0.65, during long-cycle minimum (Fig. 13). This finding could indicate that DACs are associated to the long-term periodicity. However, the correlation with their RVs is not so significant as with the orbital period (Fig. 13). We observe DACs with higher velocities after phases 0 and 0.5, followed by a monotonic decrease of their RVs; they trace a saw-teeth curve during every orbital cycle. Based on this behavior we interpret DACs as diagnostics of mass outflow from the binary. The pattern observed in Fig. 13 can easily be interpreted as DACs arising from gas streams emanating from the external Lagrangian points L_2 and L_3 . If gas accelerates through these streams following large open arcs around the binary in opposite direction to the binary motion, the observed pattern can be reproduced. Just before phase zero, we observe the weak (low density) high velocity component of the L_3 stream. Just

after phase zero we observe the strong (high density) low velocity component of the L_2 stream.

We conclude that the absorption lines observed in the infrared spectra of OGLE05155332-6925581 show a complex and variable structure, completely different to those observed in normal B-A type stellar atmospheres (Groh et al. 2007), and that our observations can be interpreted as evidence of mass loss in the binary system through the L_2 and L_3 points.

3.4 The optical spectra, radial velocities and stellar masses

The average SMARTS optical spectrum shows H I and He I absorption lines (Fig. 14). We also detected Si III λ 4553 Å, and O II $\lambda\lambda$ 4070 and 4416 Å. A list of detected features is given in Table 6. The TiO bands usually found in K0–M2 giant/supergiant stars probably arise from the nearby companion included in the slit. The presence of the O II 4070 lines indicate a forming region of high temperature and the ratio $4387/4416 \sim 1$ is indicative of high luminosity. This finding suggests the existence of a high temperature interacting region as seen in some Algol-type systems. From the inspection of the individual spectra we realized that they are highly variable: the helium and oxygen lines sometimes are visible and sometimes disappear. The equivalent widths of the Balmer lines change notoriously; we find that spectra taken around phase 0.5 show weaker Balmer lines than those observed around phase 0.0, consistent with a secondary star responsible for most of the H I absorption. We calculated the sum of the squared differences between individual spectra and the average spectrum to analyze the wavelength dependence of variability. The result is that the variability is concentrated on the Balmer lines. No emission lines were detected in the optical region in these medium resolution spectra.

The high resolution MIKE spectrum shows asymmetrical H I absorption lines and $\text{H}\alpha$ appears weakened and with a narrow emission component of $FWHM = 1.03$ Å at $\lambda = 6568.24$ Å (Fig. 15). It is not clear if the H I line asymmetry is due to blending of H I lines of the primary and secondary star or it is due to the presence of a central P-Cygni type absorption-emission minicomponent as suggested by the $\text{H}\alpha$ line. We failed to separate components with multi-gaussian deblending. Fig. 16 shows that SMARTS helium lines tend to appear during superphases 0.3-0.5. Accordingly, no helium line (neither other type apart hydrogen) was observed in the MIKE spectrum.

Radial velocities of the hydrogen lines based on SMARTS spectra are displayed in Fig. 17 along with the OGLE photometry. To our surprise, we observe that the velocities trace the motion of the secondary; the cooler component. This fact is consistent with our finding in Section 3.2 of a more luminous secondary star in the optical. The parameters of the best fitting sinus functions are given in Table 7. The optical radial velocities can be fitted with sinusoids with half amplitude between 122 ± 16 km/s ($\text{H}\beta$) and 134 ± 15 km/s ($\text{H}\delta$). The γ velocity is ≈ 275 km/s consistent with objects in the LMC. The radial velocities of the infrared lines, measured at minimum of absorption profile follow the same behavior that the optical lines, but with larger amplitude (167 ± 10 km/s for $\text{Pa}\beta$ and 152 ± 25 km/s for $\text{Pa}\gamma$) and also with surprisingly large γ (Table 7). The primary contributes to the H I line motion in opposite direction to the secondary star, then the measured RV amplitude should decrease, and this effect would be larger in low resolution spectra, as observed. The fact that the optical and infrared lines differs in the RV zero point is puzzling, and cannot be due to instrumental effects, as demonstrated by the unshifted position of telluric lines in the infrared raw spectra and the consistent optical RV with two

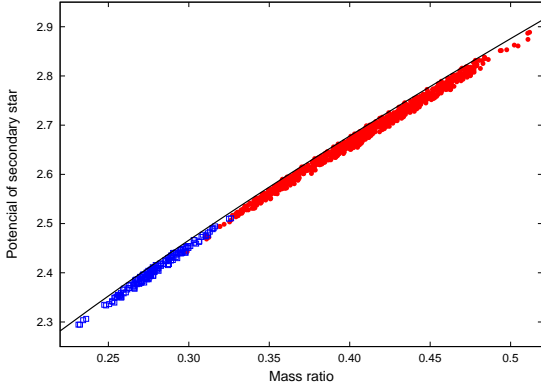


Figure 9. Mass ratio vs. potential of the secondary component. Only the best models are shown (the black points of previous figures). Parameters for OGLE fits are shown as solid circles, squares indicates MACHO blue models. The black line is a critical potential for object filling Roche lobe. Our results of Monte-Carlo simulations indicate a semi-detached configuration for OGLE05155332-6925581.

different instrumental setups. We note that the γ shift is quite similar for both Paschen lines, cannot be explained by line blending and is stable through several months for every line set. We cannot explain this γ shift at present.

The mass function for a binary in a circular orbit can be expressed as:

$$\frac{m_2 \sin^3 i}{q(1+q)^2} = 1.0361 \times 10^{-7} K_2^3 P [\text{M}\odot] \quad (2)$$

where K_2 is the half-amplitude of the RV of the secondary star measured in km/s and P the orbital period in days. Using the best fit parameters for the OGLE light curve and $K_2 = 167 \pm 10$ km/s from the infrared Pa β dataset (those with the lower scatter) we obtain masses $M_2 = 2.8 \text{ M}\odot$ and $M_1 = 7.1 \text{ M}\odot$. If we use the average K_2 of Table 7 (140 ± 20 km/s) we obtain 1.6 and $4.2 \text{ M}\odot$.

3.5 Differential-slit and wide-band photometry

We performed differential slit photometry aimed to detect the amplitude of the long-term variability in the infrared. The observing conditions were optimal to compare the spectral flux of OGLE05155332-6925581 with their nearby companion placed simultaneously in the slit. Our observations were conducted under conditions of photometric sky, we used a wide slit and the seeing was always below 0.8 arcseconds. We obtained instrumental magnitudes in the different spectral regions defined as $-2.5 \log I$ where I is the sum of spectral counts (ADUs) in the regions j, jplus and sz. The central wavelengths were chosen at 1.085, 1.295 and $1.184 \mu\text{m}$ and the band widths 0.020, 0.025 and $0.025 \mu\text{m}$. After checking for possible slit misalignments and detector noise characteristics we realized that the error of these magnitudes is mainly due to photon noise, and neglectable in all cases. When analyzing the magnitudes, we assumed that the short-term variability in the infrared had the same amplitude and behavior that in the I -band and removed this component obtaining only the long-term infrared magnitudes. Our magnitudes are plotted along with the I magnitudes in Fig. 18. A vertical shift was applied to minimize the scatter with the I magnitudes. Our data suggest that there is not significant amplitude dif-

ference of the long-term variability in the J -band comparing with the I -band LC.

It is difficult to make an analysis of the broad-band photometry due to the composite nature of the spectral energy distribution (SED) and the intrinsic variability of OGLE05155332-6925581. All photometric fluxes vary according to the long and short periodicities and in any time the total flux in any band is due at least to both stellar components plus the source causing the long-term variability. To have a rough idea about the SED properties we used the UBV photometry by Zaritsky et al. (2004) to calculate an effective reddening free parameter $Q = -0.526$ which gives $(B - V)_0 = -0.186$ (Johnson & Morgan 1953) and therefore $E(B - V) = 0.174$. The unreddened effective color corresponds to a B4 III star (Fitzgerald 1970). The color excess is comparable with the expected in the direction of the *LMC*, namely $E(B - V) \sim 0.17$ (Zaritsky 2004). On the other hand the infrared colors derived from Ita et al. (2004), viz. $(J - K) = 0.096$ and $(H - K) = 0.076$, are too red for AB-type stars; $(J - K) = -0.08$ and $(H - K) = -0.02$ and 0.02 for B5 and A5 stars, respectively (Koornneef 1983). This result is also revealed in the spectral energy distribution through multiwavelength broad-band photometry (Fig. 19). This figure shows that the optical spectral distribution at maximum light is best represented by the 20,000 K model, roughly consistent with comparable contributions of both stellar components at this phase. The infrared data, although not necessarily obtained at maximum as the optical one, clearly indicates that there is a significant infrared excess. This color excess seems to increase beyond $2.2 \mu\text{m}$, obviously cannot be reproduced by any of the binary stellar components and probably comes from the cool circumbinary disc responsible of the long-term variability.

Our models indicate that the secondary star contributes about seven times more light than the primary in the MACHO-blue band at phase zero. If we use the fact that the system has $V = 16.12$ at minimum and assume a distance modulus for the *LMC* of 18.39 ± 0.05 (van Leeuwen et al. 2007) and a color excess of $E(B - V) = 0.17$, we get $M_V = -2.83$ for the secondary star, close to the spectroscopic estimate. Among semidetached Algols, only V 356 Sgr (B3V+A1-2III; Budding et al. 2004, Ibanoglu et al. 2006) has a secondary more luminous than this. The mass-luminosity relationship for main sequence massive stars $L \sim M^{2.76}$ (Vitrichenko, Nadyozhin and Razinkova 2007) implies in our case a mass of $12.9 \text{ M}\odot$. Since the dynamical mass is much lower, this result suggests that the secondary star could be much overluminous.

For a star filling their Roche lobe the mean density is constrained by the orbital period for $q \leq 0.8$ (e.g. Frank, King and Raine 2002):

$$\bar{\rho} \cong 110 P_{hr}^{-2} \text{ g cm}^{-3} \quad (3)$$

In the case of OGLE05155332-6925581 we find $\rho = 3.6 \times 10^{-3} \text{ g cm}^{-3}$ or $\log \rho / \rho_\odot = -2.59$. Using the formula for the Roche lobe radius of the secondary star (Eggleton 1983):

$$\frac{R_2}{a} = \frac{0.49 q^{2/3}}{0.6 q^{2/3} + \ln(1 + q^{1/3})} \quad (4)$$

we found R_2 equal to $0.28a$ and $0.30a$, for $q = 0.29$ and $q = 0.39$, respectively. As the ratio between the stellar radii is ≈ 1.85 , we get $R_1 \approx 0.16a$. If we use $R_1 = 7R_\odot$ for the primary star we get $a \approx 44 R_\odot$ and $R_2 \approx 13 R_\odot$. The critical velocity for this primary is about 370 km/s.

Table 6. Lines detected in the average optical spectrum of OGLE05155332-6925581. The symbol † indicates probable lines of the nearby companion.

λ	line	λ	line
3908.7	Si I 3906†	4474.4	He I 4471
3935.2	Ca II 3934	4717.1	He I 4713
3973.2	H ϵ	4537.4	Ti I+Ti II 4533†
4105.4	H δ	4556.0	Si III 4553
4014.5	Ti I+Fe I 4010†	4865.5	H β
4028.7	He I 4026	4924.9	He I 4920
4074.6	O II 4070	4969.1	Mn I 4966†
4146.9	He I 4143	5003	TiO band 5003†
4344.4	H γ	5170	TiO band 5167†
4390.4	He I 4388	5274.8	Ca I+Fe I 5270†
4420.3	O II 4416		

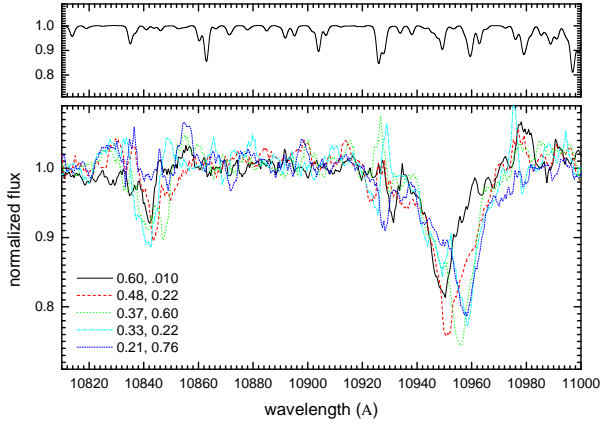


Figure 10. Pa γ and He I 1.083 μ m line profiles (down) and telluric template (up). Orbital (left) and supercycle (right) phases are indicated. Note the discrete absorption features at the blue wing of the Pa γ line.

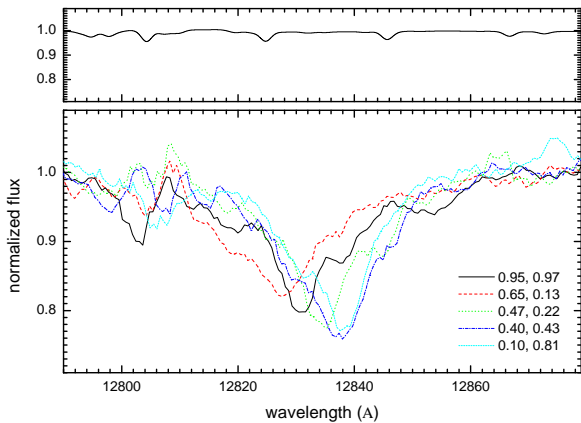


Figure 11. Pa β line profiles (down) and telluric template (up). Orbital (left) and supercycle (right) phases are indicated. Note the discrete absorption features at the blue wing of the Pa β line.

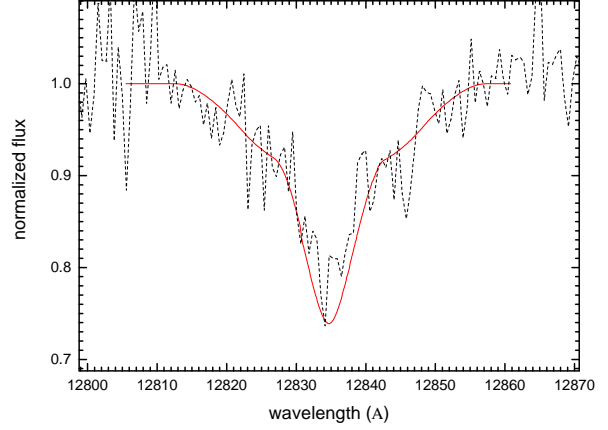


Figure 12. The Pa β line profile at phase 0.47 (superphase 0.22) along with the synthetic binary profile built considering $vsini_1 = 400$ km/s, $vsini_2 = 100$ km/s and the parameters given in the text.

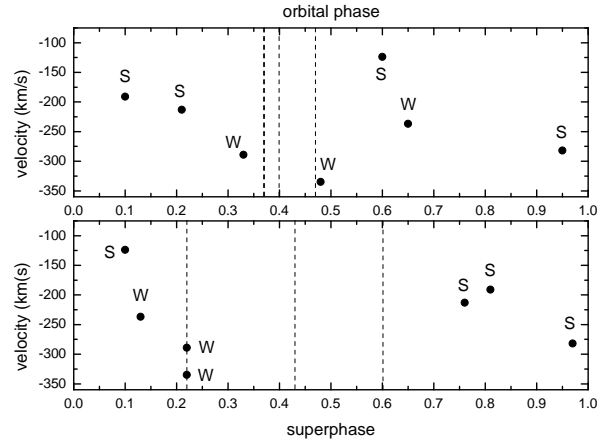


Figure 13. Radial velocities for the discrete absorption components. We label weak (W) and strong (S) lines. Dashed lines indicate very weak or absent lines.

4 DISCUSSION: PROPOSED SCENARIO AND RELEVANCE FOR DPVS

The shape of the light curve could indicate that OGLE05155332-6925581 is a semi-detached binary of the Algol type. In these binaries the less massive star appears more evolved than the more massive one, a fact that is explained if the former was initially the more massive star, evolved first and then

Table 7. Results of the fits to the RV curves in km/s.

Line	γ	K_2	Line	γ	K_2
Pa β	347 ± 5	167 ± 10	H γ	271 ± 13	123 ± 18
Pa γ	380 ± 18	152 ± 25	H δ	277 ± 11	134 ± 15
H β	280 ± 12	122 ± 16			

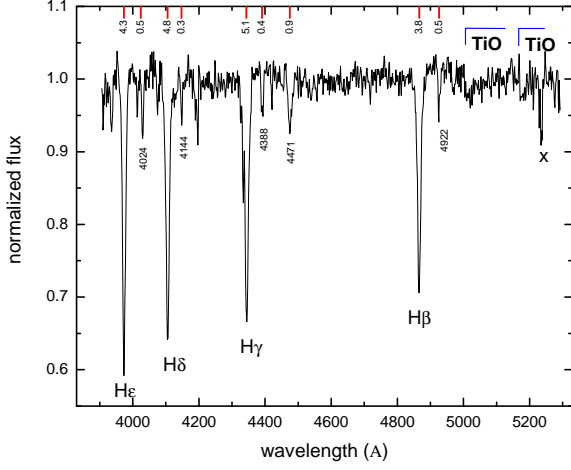


Figure 14. Normalized average SMARTS spectrum with labels and equivalent widths (in Å) for the main lines. The cross indicates a bad pixel region.

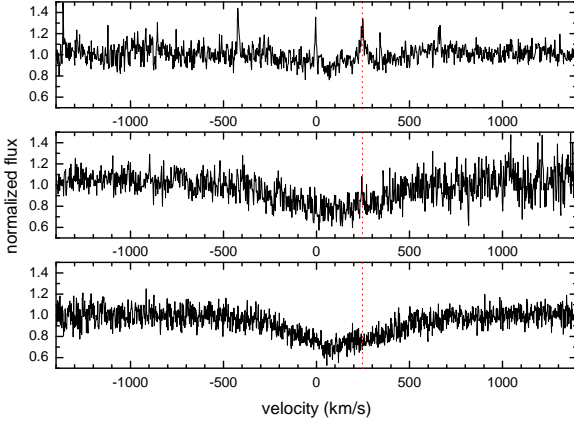


Figure 15. Normalized high resolution MIKE spectra around $H\alpha$, $H\beta$ and $H\gamma$ (from up to down) taken at orbital phase 0.756. The velocity zeros represent the laboratory rest wavelengths. Note the narrow emission feature inside the weakened $H\alpha$ absorption and the asymmetry of $H\beta$ and most notably $H\gamma$. The vertical dotted line indicates the velocity of the $H\alpha$ emission maximum.

has become the less massive star by processes of mass loss and mass transfer. The system OGLE05155332-6925581 apparently fulfills this criteria, since it shows $q < 1$ and the secondary star in an advanced stage of evolution filling their Roche Lobe. This interpretation, if confirmed, could be relevant, since very few Algols have been found in the OGLE database of the Magellanic Clouds (Wilson 2004).

4.1 On the circumpriary disc luminosity and mass ratio

We have constrained the mass ratio using the knowledge of the distance, orbital period, inclination angle, half-amplitude of RV,

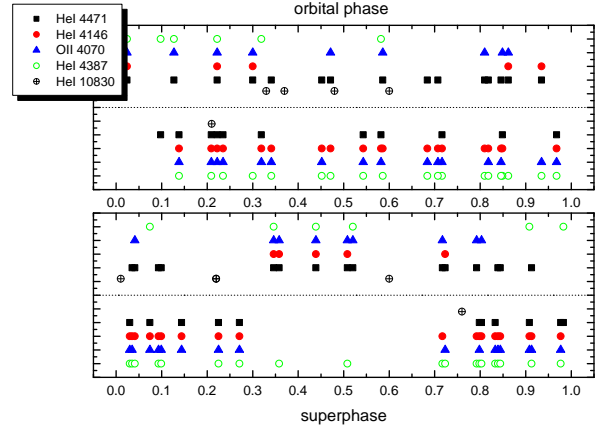


Figure 16. Presence (points above the dotted line) or absence (points below the dotted line) of Helium and Oxygen lines as a function of the orbital phase and superphase.

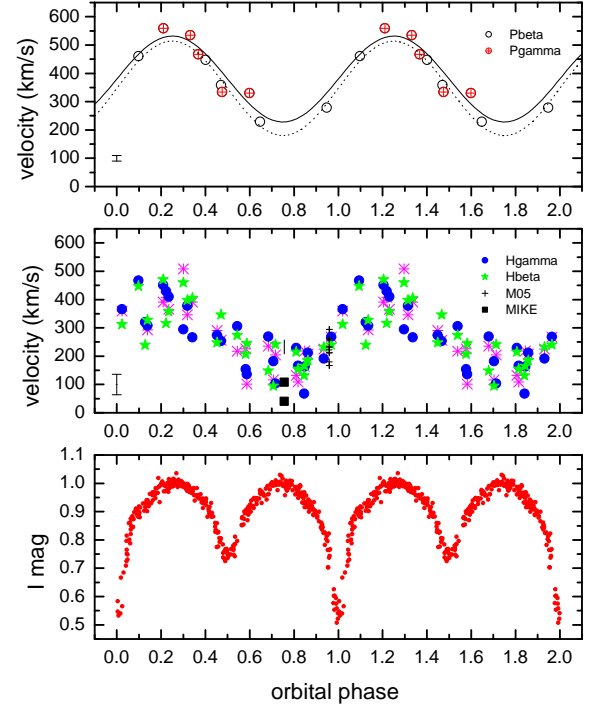


Figure 17. Radial velocities and I -band magnitudes folded with the orbital period. The best sinus fits are also shown. The vertical bars indicate the single measurement errors derived from the rms of the standard star radial velocities. Note the γ shift between optical and infrared lines. MIKE velocities correspond to the $H\gamma$ minimum and $H\gamma$ gaussian fit minimum from the lower to the higher velocity. The velocity of the peak of the $H\alpha$ emission is indicated by a vertical dash.

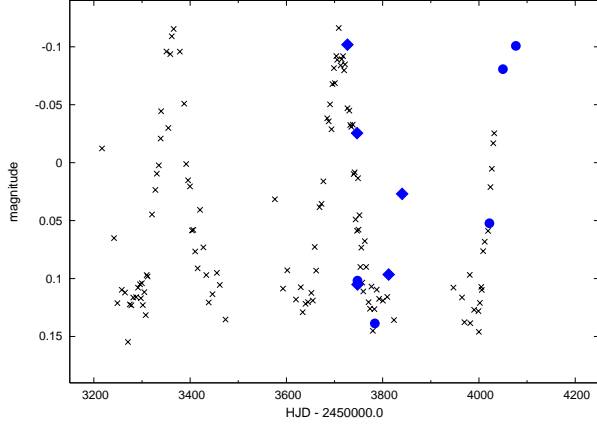


Figure 18. Long-term OGLE III *I*-band light curve along with differential spectrophotometric magnitudes *m_j* (diamonds) and *m_{jplus}* (filled circles).

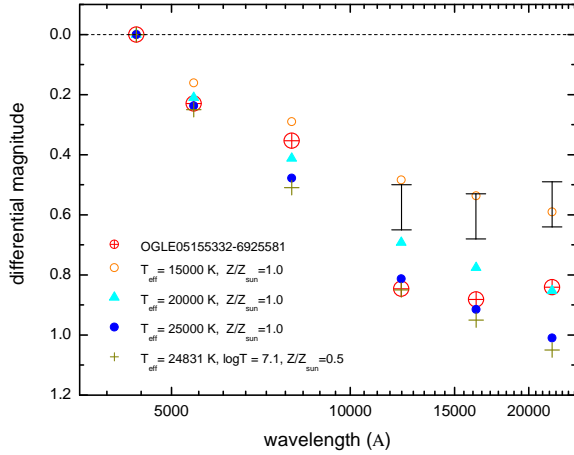


Figure 19. Simultaneous *BVI* magnitudes obtained at maximum and simultaneous *JHK* magnitudes relative to the *B* magnitude. The magnitudes have been dereddened using $A_V = 0.17$. We also show solar metallicity models from Bessell et al. (1998, for $\log g = 3.0$) and a low metallicity model from Bertelli et al. (1994). The bars indicate the 90% probability loci for *JHK* magnitudes at maximum based on Monte-Carlo simulations, i.e. the knowledge that they were obtained from the average of 10 randomly distributed images (Ita et al. 2004) and the assumption that the OGLE II light curve can be used as a seed for randomly generated infrared light curves. The figure shows that the best model for the *BVI* magnitudes at maximum is that with $T = 20,000$ K, and that there is a color excess already at the *I*-band that is prominent in redder passbands.

temperature of the secondary, assumption of spherical geometry, semidetached configuration of the system and calculated fractional light of the components. From the later and observed $M_V = -3.52$ we estimate $M_{V,1} = -2.52$ and $M_{V,2} = -2.96$ as the upper limits for the stellar magnitudes. They should correspond to the stellar magnitudes in the case of pure stellar models and zero disc light contribution. Then we calculated the theoretical $M_{V,1}(M_1(q, K_2, i, P), Z)$

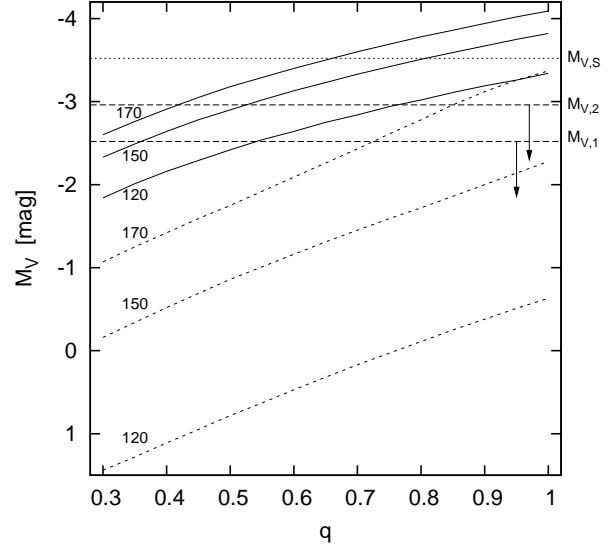


Figure 20. The q -magnitude diagram showing dynamical and model constraints for both stellar components. The horizontal lines labeled M_S , $M_{V,2}$ and $M_{V,1}$ indicate the absolute magnitude of the system, secondary and primary star, respectively, for the case of a pure stellar binary (i.e. non disc). In the real world these are upper limits since they include unknown contributions from the circumprimary and circumbinary discs (this uncertainty is showed by arrows). The oblique dashed lines represent allowed primary star M_V for three different K_2 values. These data comes from dynamical considerations. The oblique solid lines show the secondary star M_V values for the same set of RV half amplitudes. These data comes from modeling of the secondary star as a filling Roche-lobe component with fixed $T_{eff} = 12,500$ K (lower limit). See Section 4.1 for details.

and $M_{V,2}(\bar{\rho}_2(P), T_2, M_2(q, K_2, i))$ for a set of K values assuming a main-sequence mass-luminosity relationship plus stellar evolution models (Bertelli et al. 1994) for the first case and the mean density of a Roche-lobe filling star plus bolometric corrections given by Bessel et al. (1998) in the second case. We used $Z = 0.008$ and $E(B - V) = 0.17$.

Fig. 19 shows our results in the more stringent case of the low temperature limit of $T_2 = 12,500$ K. To interpret the diagram we assume that the third-light contribution is neglectable but not those of the circumprimary disc. In this case, it is evident that the $q > 1$ case is rejected, as can be easily seen in the behavior of the solid K_2 lines that cut the $M_{V,2}$ horizontal line at q values lower than ≈ 0.75 , that corresponds to the K_2 value of 120 km/s. At this point we note that the diagram can be used as a diagnostic for the circumprimary disc luminosity too. For the case of $K_2 = 120$ km/s and looking the corresponding dashed line we observe that the disc contribution should be about 2.5 magnitudes to the disc+primary subsystem. On the other hand, if K_2 is 170 km/s then $q \sim 0.4$ and the disc contributions is about 1 magnitude to the disc+primary subsystem. In all cases we observe the disc more luminous than the primary star which could explain the absence of observed primary star features in the system.

4.2 Comparison with the β Lyr system

One could ask if the disc around the primary is so optically thick that partially or completely blocks the radiation from the embedded star, in a similar way that happens in β Lyr (Wilson 1974). In this view the primary eclipse is mainly from the disc, not the primary.

If the disc is the main source eclipsed during main eclipse, and its brightness is fully accretion powered and comparable in luminosity to the secondary star, then the mass accretion rate should be related to its luminosity through:

$$L_{disc} = \frac{GM_1}{R_1} \frac{dm}{dt} \sim L_2 \quad (5)$$

Using an approximated mass-radius relation for main sequence stars $R_1 = R_\odot (M_1/M_\odot)^{0.7}$, the $M_V = -2.83$ for the secondary star derived above and $BC = -1.2$ for a 14,000 K star, we obtain $dm/dt \sim 1.03 \times 10^{-4} (M_1/M_\odot)^{-0.3}$, weakly dependent on the primary star mass. For $M_1 = 7M_\odot$ we get $dm/dt \sim 5.7 \times 10^{-5} M_\odot/\text{year}$. In the conservative case of mass transfer, we should observe an orbital period change given by:

$$\frac{\dot{P}}{P} = \frac{3\dot{m}(m_1 - m_2)}{m_1 m_2} \quad (6)$$

(e.g. Hilditch 2001). For the stellar masses estimated in Section 3.4 we obtain $\frac{\dot{P}}{P} = 2.9 \times 10^{-5}$, being the observed upper limit 4×10^{-6} . The lack of detected orbital period variability suggests a minor role of accretion to the systemic luminosity. As the disc seems to be luminous, it is possible that it is heated by other mechanisms apart from accretion.

4.3 Possible evolutionary stage

The initially more massive star of a close binary fills their Roche lobe during one of three possible phases (Kippenhahn and Weigert 1967): during core hydrogen burning (Case A), H-shell burning (Case B) or He-shell burning (Case C). The fact that we observe a hydrogen secondary star in OGLE05155332-6925581 would indicate that the system is the result of a Case A or Case B mass exchange. Calculations of the evolution of a close binary component of $9 M_\odot$ during Case A mass exchange show a short phase of fast mass loss (at rates $\sim 10^{-3} M_\odot/\text{year}$) from the initially more massive star lasting $\sim 6 \times 10^4$ years, after which the star loses a large fraction of their initial mass, reaching $3.73 M_\odot$ (Kippenhahn and Weigert 1967). During this phase the system loses matter and angular momentum through the L_2 point forming a Keplerian ring located at $\approx 2.25 \times a$ (Soberman et al. 1997). As this ring carries a lot of mass and angular momentum the result is an important decrease of the orbital period. As we do not observe this rapid period change in OGLE05155332-6925581, the system is probably after this rapid stage, in the $q < 1$ regime, consistent with our photometric mass ratio and conclusion of Section 4.1. The computations by Kippenhahn and Weigert (1967) show that after this rapid stage mass loss continues but is very slow and limited to mass transfer from the secondary to the primary at rates $\sim 4 \times 10^{-8} M_\odot/\text{year}$. If the system is in this stage, accretion is not enough to power the disc with the observed brightness.

4.4 On the long-term variability and circumbinary disc

The non-eclipsing nature of the long variability places their origin outside the binary system, probably in a circumbinary disc. It is

highly likely that this disc is also responsible for the observed infrared excess. We note that this disc is probably not the fossil of the disc formed during the phase of rapid mass loss by the binary, since we found evidence that the disc is not permanent and that new material is being constantly supplied by the binary. We propose that gas is being expelled outside the binary through the L_2 and L_3 points. The DACs pattern of Fig. 13 strongly supports this view and indicates that the gas accelerates through the streams in open arcs around the binary in opposite directions to the orbital motion feeding the circumbinary disc. It is possible that the remnants of the earlier stages of the evolution form an extensive structure around the system modifying the observed properties of the object (e.g. colors). Further observations in the far infrared and radio wavelengths should be useful to check this view.

The loop encountered in the CM diagram could provide a key to understand the cause for the long term variability. Similar loops have been found in SMC Be stars (de Wit et al. 2006), being interpreted in terms of Brehmstrahlung emission arising from cycles of disc formation and dissipation around Be stars. De Wit et al. (2006) showed that loops in the CM diagram appear when optically thick discs are formed by stellar mass ejections and then dissipate as optically thin rings into the interstellar medium. In the same way, the CM loop observed in OGLE05155332-6925581 could indicate the formation of an outflowing optically thick circumbinary disc and their posterior dissipation in the form of an optically thin ring into the interstellar medium. Cycles of disc expansion/contraction are probably excluded by the LC shape with prolonged minima. The correlation found in DPVs between the orbital and long period (Mennickent et al. 2003) suggests that the mass loss is modulated by some kind of instability inside the binary system.

It has been shown by Packet (1981) that during mass exchange in a closed binary system, enough angular momentum is transferred toward the mass accreting star to spin it up to its critical rotational velocity after gaining only a small percentage of its original mass. Hence, the primary of OGLE05155332-6925581 could be rotating at their critical velocity (see also de Mink et al. 2007). Our observations of a rapidly rotating primary support this view. In this case additional gas supplied by the secondary could form a disc around the primary. The residuals observed in the LC models, the $H\alpha$ emission, the changing He I lines and eventually the suspected line emission shoulders, could be evidence of a disc plus interacting region. We propose that this disc fills the Roche lobe of the primary and escapes through the L_3 point. If the system has a low mass ratio, the disc could grow beyond the 3:1 resonance radius (Lubow 1992, Murray 1996) and precession could help to funnel material through the L_3 point (Mennickent et al. 2003). The behavior of the helium lines, which are detected primarily during long cycle minimum, is compatible with the occultation (or depletion) of the interacting hot region during episodes of strong mass loss from the binary.

5 CONCLUSIONS

In this paper we have analyzed the eclipsing double periodic variable OGLE05155332-6925581 arguing that it could be a clue to understand the phenomenon of Double Periodic Variables. We find a set of physical parameters best fitting the multiwavelength light curves and find a much improved value of the orbital period. Our LC and dynamical analyses indicate that OGLE05155332-6925581 is a semi-detached binary with intermediate mass components where the less massive star transfers

matter onto the more massive star. We detected evidence for a luminous disc of gas around the primary as in β Lyr. However, OGLE05155332-6925581 does not show changes in the orbital period as β Lyr does. We argue that the main powering source for the disc probably is not accretion. We speculate that gravitational tidal forces could maintain the disc heated and eventually contribute to expel mass from the system. Other explanations for the constancy of the orbital period based on competing mechanisms producing mutually canceling effects of orbital shrinking and period increase seem to be highly unlikely. In our view the system is found after a rapid mass exchange associated to Case A or Case B mass transfer, where the secondary star appears undermassive and overluminous due to the erosion of their outer layers by the mass loss processes.

We find evidence for a variable circumbinary disc, that should be the cause of the long-term periodicity and the infrared excess. Remarkably, the long-term variability follows a loop in the CM diagram indicating quasi-cyclic episodes of disc creation/dissipation; the mass loss being modulated by some still unknown process in the binary. The remarkable discovery of DAC RVs following a saw-teeth pattern during the orbital cycle strongly supports the view that mass is being lost from the system through accelerated streams arising from the Lagrangian L_2 and L_3 points. This should be the source of mass for the circumbinary disc. We conclude that OGLE05155332-6925581, and probably all DPVs, are intermediate mass semidetached Algol type binaries in a evolutionary stage characterized by mass exchange, mass loss and circumbinary discs. DPVs look more massive, bluer and more luminous than classical Algols; their study is potentially important to constraint non-conservative models of massive binary star evolution.

Despite of the significant advances in the knowledge of DPVs provided by the study presented in this paper, we are certain that problems with the complete interpretation of the phenomenon still persist. The complex and variable nature of OGLE05155332-6925581 requires better quality and more extensive observational material than we have collected. Firstly, we do not know what is the mechanism driving and regulating the long cycle variability. In addition, the identification of detected spectral features with specific places in the system and its environment is still uncertain, especially for the $H\alpha$ emission. We do not know how important is the role of the mass transfer and fast rotation of the primary star in the mechanism driving the long cycle variability. The interesting γ shift observed between optical and infrared lines of the secondary still has no explanation. Finally, the basic properties (mass, size, temperature) of circumbinary disc/structure are still unknown. The recent discovered bright DPVs in the Galaxy (Kołaczowski & Mennickent, in prep.) open new opportunities to our research. We are going to extend our project for intensive, multi-instrumental study of these very promising targets. It will permit to reach the level of accuracy and time resolution essential for constructing a comprehensive model of their activity.

On the other hand, the MC DPV sample is unique in their completeness and homogeneity. For these systems we roughly know distance, total absolute magnitude and luminosity; we will continue working on this sample to provide a sound basis of comparison for the Galactic sample with the goal of getting insights on the influence of the metallicity parameter on the DPV properties. We plan also make a detailed comparison with the Galactic classical Algol stars to enlighten the DPV-Algol connection.

ACKNOWLEDGMENTS

We acknowledge the referee Dr. P.P. Eggleton for useful comments on a first version of this manuscript, especially for calling our attention on the possible importance of the circumprimary disc in modeling this system. REM acknowledges financial support by Fondecyt grant 1070705. WG, GP and REM acknowledge financial support from the Chilean Center for Astrophysics FONDAP 15010003. LC and AG acknowledges the Agencia de Promoción científica y Tecnológica for supporting this research with the grant BID 1728 OC/AR PICT 03-12720.

This paper utilizes public domain data obtained by the MACHO Project, jointly funded by the US Department of Energy through the University of California, Lawrence Livermore National Laboratory under contract No. W-7405-Eng-48, by the National Science Foundation through the Center for Particle Astrophysics of the University of California under cooperative agreement AST-8809616, and by the Mount Stromlo and Siding Spring Observatory, part of the Australian National University. NSO/Kitt Peak FTS data used here were produced by NSF/NOAO.

REFERENCES

- Allsman R. A., Axelrod T. S., for the Macho Collaboration, 2001, astro, arXiv:astro-ph/0108444
- Bertelli G., Bressan A., Chiosi C., Fagotto F., Nasi E., 1994, A&AS, 106, 275
- Bessell M. S., Castelli F., Plez B., 1998, A&A, 333, 231
- Budding E., Erdem A., Çiçek C., Bulut I., Soyduğan F., Soyduğan E., Bakiş V., Demircan O., 2004, A&A, 417, 263
- Catala C., Kunasz P. B., 1987, A&A, 174, 158
- de Mink S. E., Pols O. R., Glebbeek E., 2007, arXiv, 709, arXiv:0709.2285
- de Wit W. J., Lamers H. J. G. L. M., Marquette J. B., Beaulieu J. P., 2006, A&A, 456, 1027
- Eggleton P. P., 1983, ApJ, 268, 368
- Fitzgerald, M., 1970, A&A, 4, 234
- Frank J., King A., Raine D. J., 2002, Accretion Power in Astrophysics, Cambridge University Press
- Groh J. H., Damineli A., Jablonski F., 2007, A&A, 465, 993
- Harmanec P., 1988, BAICz, 39, 329
- Hilditch R. W., 2001, An Introduction to Close Binary Stars, Cambridge University Press
- Ibanoğlu C., Soyduğan F., Soyduğan E., Dervişoğlu A., 2006, MNRAS, 373, 435
- Ita Y., et al., 2004, MNRAS, 347, 720
- Johnson, H. L., Morgan, W. W., 1953, ApJ, 117 313
- Kippenhahn R., Weigert A., 1967, ZA, 65, 251
- Koornneef J., 1983, A&A, 128, 84
- Kurucz R. L., 1979, ApJS, 40, 1
- Lubow S. H., 1992, ApJ, 401, 317
- Mennickent R. E., Pietrzyński G., Diaz M., Gieren W., 2003, A&A, 399, L47
- Mennickent R. E., Cidale L., Díaz M., Pietrzyński G., Gieren W., Sabogal B., 2005a, MNRAS, 357, 1219
- Mennickent R. E., Assmann P., Pietrzyński G., Gieren W., 2005b, ASPC, 335, 129
- Murray J. R., 1996, MNRAS, 279, 402
- Michalska G., Pigulski A., 2005, A&A, 434, 89
- Packet W., 1981, A&A, 102, 17

- Soberman G.E., Phinney, E.S., van den Heuvel E.P.J., A&A, 1997, 327, 620
 Szymański M., 2005, AcA, 55, 43
 Udalski A., Kubiak M., Szymański M., 1997, AcA, 47, 319
 van Leeuwen F., Feast M. W., Whitelock P. A., Laney C. D., 2007, MNRAS, 379, 723
 Vitrichenko E. A., Nadyozhin D. K., Razinkova T. L., 2007, AstL, 33, 251
 Wallace L., Meyer M. R., Hinkle K., Edwards S., 2000, ApJ, 535, 325
 Wilson R. E., 1974, ApJ, 189, 319
 Wilson R. E., 2004, NewAR, 48, 695
 Wilson R. E., Devinney E. J., 1971, ApJ, 166, 605
 Wyrzykowski L., et al., 2003, AcA, 53, 1
 Zaritsky D., Harris J., Thompson I. B., Grebel E. K., 2004, AJ, 128, 1606

This paper has been typeset from a \LaTeX file prepared by the author.